Accepted Manuscript

General rights:

Confinement on the Optical Response in h-BNCs: Towards Highly Efficient SERS-active 2D Substrates

Marcos Mandado* and Nicolás Ramos-Berdullas

Department of Physical Chemistry, University of Vigo, Lagoas-Marcosende s/n, 36310.Vigo, Spain

***corresponding author email:** mandado@uvigo.es

ABSTRACT

Several experimental and theoretical studies have shown that 2D hybrid structures formed by boron, nitrogen and carbon atoms (h-BNCs) possess a highly tunable linear and non-linear optical responses. Recent advances towards the controlled synthesis of these unique structures have motivated an important number of experimental and theoretical work. In this work, the confinement on the optical response induced by boron-nitride (BN) strings in h-BNC 2D structures is investigated using time-dependent density functional theory (TDDFT) and electron density response properties. The number of surrounding BN strings (N_{BN}) necessary to "isolate" the optical modes of a carbon nanoisland (nanographene) from the remaining substrate has been characterized in two different nanoisland models: benzene and pyrene. It was found that for $N_{BN} \geq 3$ the excitation wavelengths of the optically active modes remain constant and the changes in the transition densities, the ground to excited state density differences and their associated electron deformation orbitals are negligible and strongly confined within the carbon nanoisland. Using a water molecule as model system, Raman enhancement factors of 10^6 for the water vibrational modes are obtained when these electromagnetic "hot spots" are activated by an external electromagnetic field. The high tunability of the optical absorption bands of nanographenes through changes in size and morphology makes h-BNCs be perfect materials to construct platforms for surface enhancement Raman spectroscopy (SERS) for a wide range of laser sources.

INTRODUCTION

Recent studies focused on vacancy and doped graphene featuring tunable bandgaps have opened up many possible applications of these materials in fields such as electronics, photonics and plasmonics.[1-3] In particular, a direct consequence of this bandgap tunability is reflected on the graphene optical activity as it allows shifting the plasmon emission from the THz region to the UV region,[4] improving its functionality and applicability.[5-7] Thus, these materials appear to be good candidates for the development of flexible one-atom-thick electronic and optical characteristics.[8]

Among all the 2D monolayer materials, the hexagonal boron-nitrogen-carbon (h-BNC) hybrids show a unique versatility to introduce bandgap variations in an interesting manner.[9] For years, the experimental work had focused on the synthesis of h-BNC through the use of growing techniques. Fortunately, important steps towards a reliable and controllable synthesis of h-BNCs have been taken recently,[9-12] which have stirred the interest of the scientific community in these materials and their potential applications. Meanwhile, theoretical studies have revealed an unequivocal relationship between the bandgap sizes and the h-BN patterns within the 2D surface lattice.[13-16] The high tunability of the optical response in h-BNC structures by means of modifying the size and shape of nanosized carbon and boron nitride embedded structures was previously shown by Karamanis et al.[13,14] However, theoretical efforts have focused on exploring this relationship and less attention has been paid to understand other important issues, such as the localization of the optical response, the formation of electromagnetic "hot spots" on the carbon nanoislands or the interaction of near molecules with these "hot spots". Indeed, this could be interesting for spectroscopic techniques enhanced by surfaces with plasmonic activity, such as Surface Enhanced Raman Spectroscopy (SERS), Surface

Enhanced Infrared Absorption (SEIRA) Spectroscopy and Surface Enhanced Hyper-Raman Spectroscopy (SEHRS).

The possibility of h-BNCs to be applied as substrates in Surface Enhanced Raman Spectroscopy (SERS) was suggested in a previous work,[17] due to the large polarizability enhancement displayed by the carbon nanoisland at near-resonance conditions. Thus, strong Raman enhancements arise from resonance processes, such as the electromagnetic enhancement, the most important in metals, which is related to the plasmonic activity of the substrates, and the charge-transfer enhancement, which stems from electronic excitations between surface and molecule. Another weaker enhancement is associated with the surface-molecule interaction, which is known as chemical enhancement.[18,19] It was recently found that an additional enhancement factor, the surface-molecule vibrational coupling, contributes significantly to the increase of the Raman activity on carbon substrates but marginally on substrates formed by heavier atoms, such as silver or gold nanoparticles.[20-22]

In spite of the high sensitivity reached by metallic plasmonic surfaces,[23] the search for new SERS substrates still keeps a lively interest due to the need to improve other aspects such as the molecular selectivity, the production cost, the chemical stability and the biocompatibility. Besides improving these other aspects, the new substrates should retain as much as possible the sensitivity displayed by plasmonic surfaces.

One of the most promising SERS substrates discovered in last decade has been graphene.[24-26] Its great chemical stability and adsorption capacity together with the noncovalent nature of the interactions stablished with most analytes make this substrate very attractive for SERS.[27,28] Unfortunately, the Raman enhancement factors are significantly lower with respect to metallic nanoparticles due to the lack of plasmonic activity in the UV region, which is only partially compensated by a very low detection limit.[29,30] Thus, the suitability

of graphene related structures as substrates for Raman enhancement is still being examined, on the one hand, with structure modifications, such as vacancy-defects,[31] doping[32] or functionalization,[33] and on the other hand, with metal-graphene hybrid structures,[34] exploiting both the advantages of the graphene flat surface and the plasmonic activity of the metal.

As mentioned above, an alternative way to augment the Raman enhancement factor of a graphene surface is through confinement of the optical response, such as in h-BNCs. Previous works suggested plasmonic activity in graphene molecules and polycyclic aromatic hydrocarbons (PAHs)[5,6,35] and later simulations proved that large Raman enhancements in molecules interacting with a graphene nanodisk may be reached for near plasmon resonance frequencies.[22] This work shows the same characteristics are found for carbon nanoislands within BN monolayers and stablishes the degree of confinement of the electromagnetic response within these nanoislands. Therefore, the electromagnetic "hot spots" created by the BN strings could be exploited in SERS applications or related spectroscopic techniques, improving the sensitivity of graphene based SERS where the Raman stems from charge-transfer or chemical factors.

METHODOLOGY

Two different models of carbon nanoisland were considered for this study, benzene and pyrene. The nomenclature employed in this work to denote the different h-BNCs contains the acronym Be or Py, for h-BNCs containing benzene or pyrene nanoislands, followed by the number of surrounding BN strings (N_{BN}), which varies from 0 to 5 in benzene and from 0 to 4 in pyrene. Herein, BN strings, or CC strings in an analogous nanographene structure, are referred to closed chains of alternatively arranged boron and nitrogen atoms

which added to the carbon nanoisland allow generating larger and larger h-BNC structures preserving the spatial symmetry. This symmetry preservation is the reason for using these strings, particularly N_{BN}, to study the size effects on the optical response. The structures with the largest N_{BN} (Be-5 and Py-4) are shown in Figure 1, BN strings are also remarked with solid black lines. All the h-BNC structures were optimized using density functional theory (DFT) with the CAM-B3LYP functional and the split valence doubly polarized 6-31G(d,p) basis set. This functional choice was based on its suitability for the study of systems with strong π-electron delocalization,[36] calculation of optical response properties[37] and characterization of excited states.[38] This functional was also the choice in previous studies of h-BNCs.[13-15] The basis set chosen is not as large as desired and includes polarization functions but not diffuse functions in order to reduce the considerable computational cost expected for the largest systems studied. A similar basis set was also the choice in previous theoretical studies of the optical response in h-BNCs.[13-15] Frequency calculations confirmed that all the energy minima correspond to perfectly planar structures, with D_{3h} and C_{2v} symmetries for Be-N_{BN} ($N_{BN} > 0$) and Py-N_{BN} ($N_{BN} > 0$), respectively.
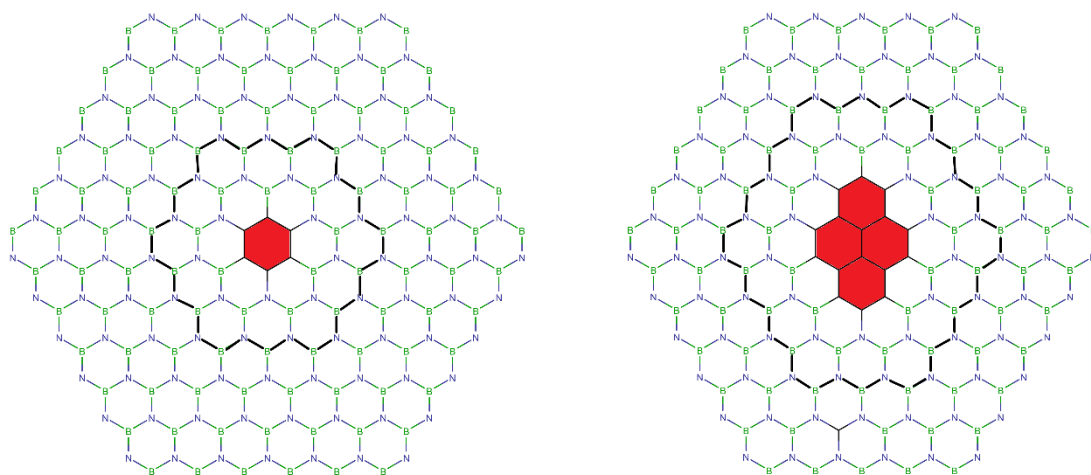
Fig 1. Largest h-BNC structures considered in this work (Be-5 and Py-4). Carbon nanoislands are highlighted in red and a BN string is remarked with solid black lines. Peripheral hydrogen atoms are not shown.

As mentioned in the previous section, the study was split into two parts. In a first step, the first twenty excited states of each h-BNC structure were obtained using time-dependent density functional theory (TDDFT) and the same functional+basis set employed for the geometry optimization of the ground state. Vertical excitation wavelengths, transition dipole moments and oscillator strengths were calculated with the Gaussian09 program,[39] the same software employed for the geometry optimizations. Afterwards, the transition density (TD), local transition dipole moments (LTDMs) for the carbon nanoislands, ground to excited state density difference (DD) and electron deformation orbitals (EDOs) associated with the DD were obtained for each optically active mode by means of an own Fortran code. Plots of TDs and DDs were drawn with Gaussview 5.0.[40] Extensive theoretical information about the definition of LTDMs and EDOs is given as Supporting Information.

In a second step, Py-N_{BN} structures were employed as model to check the capability of h-BNC carbon nanoislands to enhance the Raman activity (RA) of molecules adsorbed on their surfaces. A water molecule was selected for this part of the study due to its reduced size, which perfectly fits within the pyrene boundaries, and its simple Raman spectrum. This spectrum consists of three Raman-active vibrational modes; the symmetric and asymmetric O-H bond stretchings and the symmetric bending. RAs were calculated using off- and on-resonance conditions with the couple perturbed density functional theory (CPDFT) by means of the Gaussian09 program. For the on-resonance simulations, electromagnetic perturbations with wavelengths detuned 2 nm with respect to the resonance wavelengths in each of the two most active excitation modes were introduced in the calculations.[41,42] These excitations correspond to two perpendicular in-plane

polarized modes. Thus, each represents a different kind of optical excitation in terms of symmetry. The corresponding Raman spectra were plotted using Lorentzian lineshapes with a half-height width of 5 cm^{-1} with the help of Gabedit 2.4.8 graphical interface.[43]

In order to get insight into the role played by molecule-surface vibrational couplings in the Raman enhancement, the RAs were split into molecule and surface terms according to their respective contributions to the vibrational modes (see reference 20 for details). Hypothetical spectra obtained by removing the surface contributions from the RAs were generated and confronted to the full spectra.

**RESULTS AND DISCUSSION**

Confinement on the Optical Response

The smallest carbon nanoisland that can be thought for a h-BNC structure is benzene. It is well known that the electronic absorption spectrum of benzene shows a strong band centred around 178 nm. This corresponds to the excitation of two in-plane degenerated modes of E_{1u} symmetry. Our TDDFT calculations predict a slightly smaller excitation wavelength for these modes (165 nm). From a MO view, these excitation modes arise from the combination of single electron excitations from one of the doubly-degenerate HOMO (H) to one of the doubly-degenerate LUMO (L). The effect of surface enlarging, either introducing CC or BN surrounding strings, over the L-H energy gap, excitation wavelength and oscillator strength is shown in Fig. 2. As it can be observed, the excitation wavelength increases linearly with the number of CC strings in the pristine graphene nanodisks, which is the consequence of the progressive decay of the L-H gap. On the contrary, both the L-H gap and, consequently, the excitation wavelength do not change with the number of BN strings for nanodisks with $N_{BN} \geq 3$. Interestingly, the excitation intensity, as measured by the oscillator strength, increases linearly both with the number

of CC and BN strings. Even though the oscillator strength is substantially larger in pristine graphene nanodisks, it also shows a continuous growth in Be-N_{BN}, giving rise to stronger signals as N_{BN} increases but, contrary to graphene nanodisks, the optical response seems to be locked within the same surface area. For comparison, the L-H energy gaps obtained for analogous h-BN nanodisks are also included in the plot. As can be observed the gap also decreases monotonically with the number of BN strings, although this decrease is significantly less pronounced than in graphene nanodisks and the gap values are much larger. This is the expected result taking into account the well-known finite band gap of a BN monolayer (also known as white graphene) contrary to the zero gap displayed by graphene. Comparing the other two magnitudes represented in Fig. 2, excitation wavelength and oscillator strength, for h-BN does not make as much sense since they correspond to electronic excitation modes located on the central carbon nanoisland, which does not exist in the pure h-BN structures.
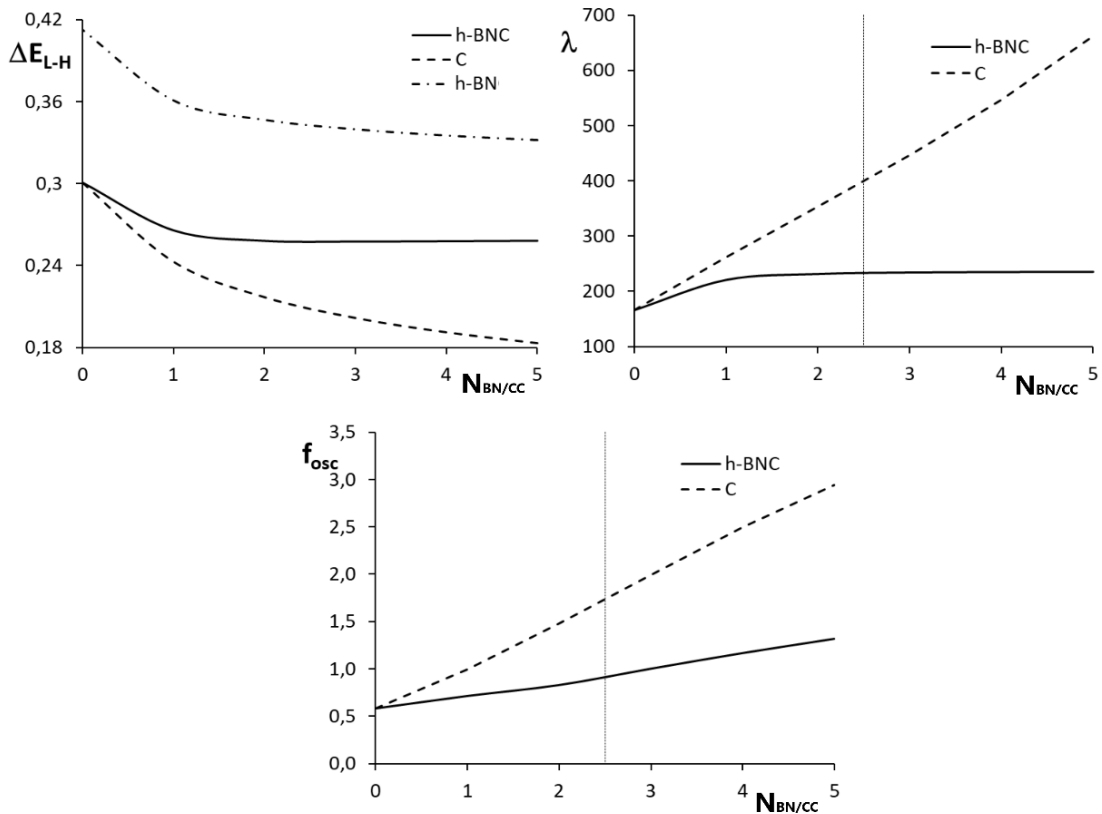
Fig 2. LUMO-HOMO energy gap (top-left), $\Delta E_{\text{L-H}}$, excitation wavelength (top-right), λ, and oscillator strength (bottom), f_{osc}, vs the number of BN or CC strings, $N_{\text{BN/CC}}$, in the h-BNCs and graphene nanodisks (denoted by C in the plots) with a central benzene and analogous h-BN nanodisks.

In order to visualize the effect of the confinement, the DD associated with one of these degenerated modes has been represented in Fig 3 for graphene and Be-N_{BN} nanodisks. As can be observed, whereas the response is spread out over the whole nanodisk surface in the graphene nanostructures, it is perfectly located on the carbon nanoisland and the near surrounding atoms in the Be-N_{BN} nanodisks. In fact, the plots become indistinguishable when $N_{\text{BN}} > 2$. Notice that the isosurface values employed for the h-BNC series is always the same but it decreases with the number of CC strings in the graphene nanodisks, reflecting a local attenuation of the response in the latter. We would like to remark the effect of symmetry change from D_{6h} to D_{3h} observed in the DD plots of Fig 3 when going from Be-0 to Be-1. A very recent study showed that the change from D_{6h} to D_{3h} symmetry in nanographenes may have a drastic effect on the electronic properties. This could also introduce interesting effects in h-BNCs with larger carbon nanoislands, such as coronene and circumcoronene.[44]
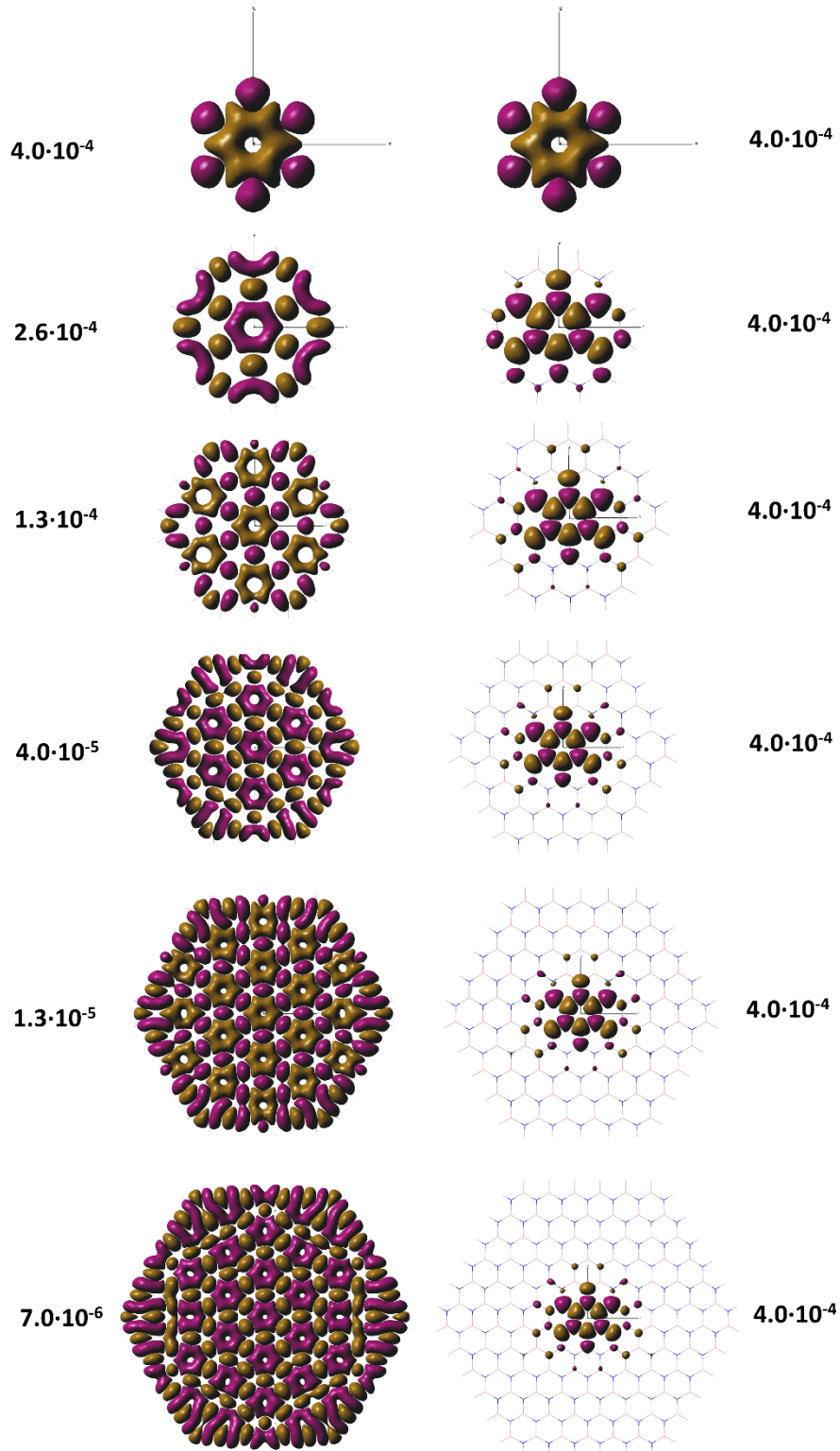
Fig 3. DDs in the h-BNCs (right) and graphene nanodisks (left) with a central benzene. The numbers indicate the isosurface value employed for each representation.

The local confinement of the electromagnetic response may be further quantified by calculating the LTDMs for the central benzene unit in both types of nanodisks. The results

are collected in Table 1. Comparing the second and third column of this table, it can be observed that the LTDM decreases monotonically with the number of CC strings in the series of graphene nanodisks, whereas its change is negligible in Be-N_{BN} when $N_{BN} > 2$. The former stems from the spreading of the excitation mode to the whole nanodisk, where the latter is a consequence of the local confinement within the benzene nanoisland and its near surroundings.

Table 1. LTDMs calculated for the central benzene and pyrene nanoislands for the strongest excitation modes. For Be-N_{BN} nanodisks the results are confronted to those obtained for graphene nanodisks.

| $N_{BN}/_{CC}$	Be-N_{BN}	Graphene	Py-N_{BN} (y)	Py-N_{BN} (z)
0	1.876	1.876	1.798	2.082
1	0.771	0.540	0.924	0.796
2	0.622	0.302	0.615	0.990
3	0.591	0.182	0.624	0.974
4	0.596	0.101	0.626	0.968
5	0.600	0.062		

The model of pyrene nanoisland introduces two elements with respect to benzene. First an enlargement of the carbon unit and second a partial symmetry loss. It is interesting to evaluate how these two elements affect the confinement of the electromagnetic response. As mentioned in the previous section, two perpendicular excitation modes have been studied in the Py-N_{BN} nanodisks, one of them polarized in the *y* direction and the other one in the *z* direction. The symmetry reduction from D_{3h} to C_{2v} breaks the degeneracy previously found for the excitation modes in Be-N_{BN}. The excitation wavelengths and oscillator strengths for these two modes are represented against N_{BN} in Fig 4. The wavelength increases for the smallest nanodisks but keeps constant for those with $N_{BN} \geq 3$, the same result found for Be-N_{BN}. On the other hand, the oscillator strength decreases with the first BN string, contrary to that found in Be-N_{BN}, but increases monotonically afterwards for nanodisks with $N_{BN} \geq 2$.
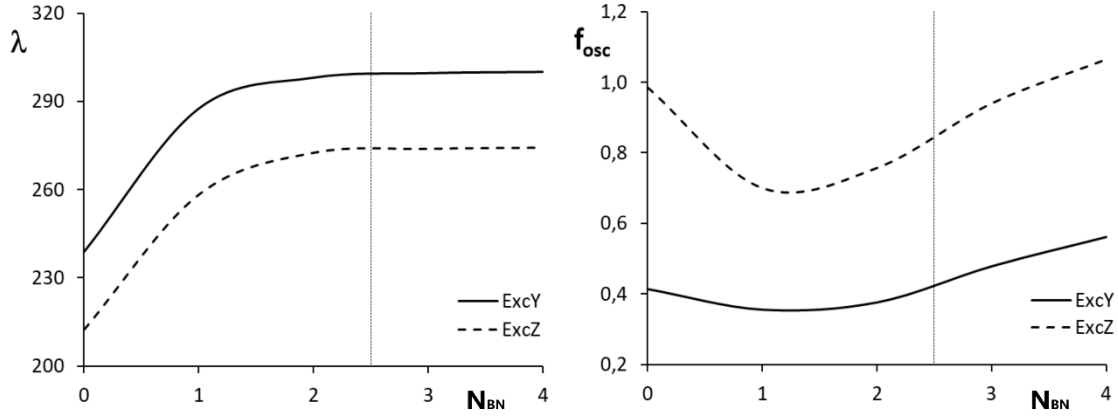
Fig 4. Excitation wavelength (left), λ, and oscillator frequency (right), **f_{osc}**, vs the number of BN strings, **N_{BN}**, in the h-BNCs with a central pyrene. The plots collect the results for the *y*-polarized (ExcY) and *z*-polarized (ExcZ) modes studied.

The LTDMs of the pyrene nanoisland are collected in Table 1 for the two excitation modes. As previously found for Be-N_{BN}, the strength of the transition dipole located at the pyrene unit decreases when one and two BN strings are added, but the change is negligible for nanodisks with $N_{BN} > 2$. This reflects that the electromagnetic response is locally confined within the pyrene unit and the near surroundings, which encompasses, roughly speaking, the first two BN strings. Inspection of the DDs and TDs for the series of Py-N_{BN} (Fig 5) confirms the outer region, including the third and fourth BN strings, contributes marginally to the response.

The TDs for the two excitation modes are represented on the right side of Fig 5. Since Py-N_{BN} nanodisks are not centrosymmetric unlike Be-N_{BN}, the *z* direction in the figure appears in the nanodisks with an odd number of BN strings inverted with respect to those with an even number. Therefore, the plots also appear inverted but the density distribution is indistinguishable for nanodisks with $N_{BN} \geq 2$. The direction of the transition dipole moment is clear on the plots. The *z*-polarized and *y*-polarized modes are shown in the third and fourth columns, respectively.
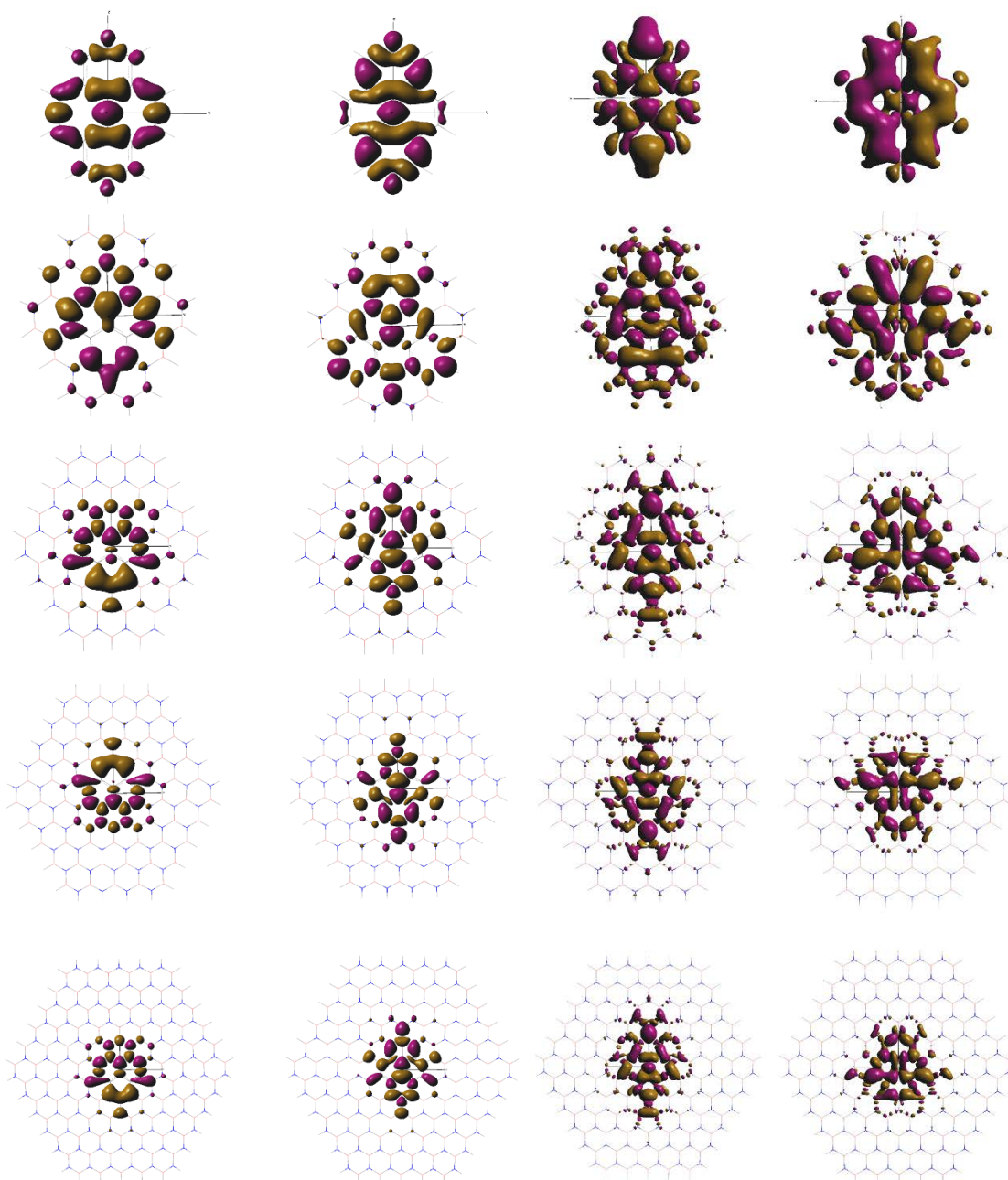
Fig 5. DD (the two columns on the left) and TD (the two columns on the right) in the h-BNCs with a central pyrene. The left and right columns of each representation correspond to the *z*-polarized and *y*-polarized modes, respectively. Isosurface values of $4 \cdot 10^{-4}$ and $1 \cdot 10^{-3}$ are used for DDs and TDs, respectively

In the MO picture that provides the KS-TDDFT, an excitation mode is the result of the combination of single electron excitations/deexcitations between occupied and virtual MOs, the relative weight of each is given by the square of the coefficients of the corresponding excitation/deexcitation in the solution of the Casida equation.[45]
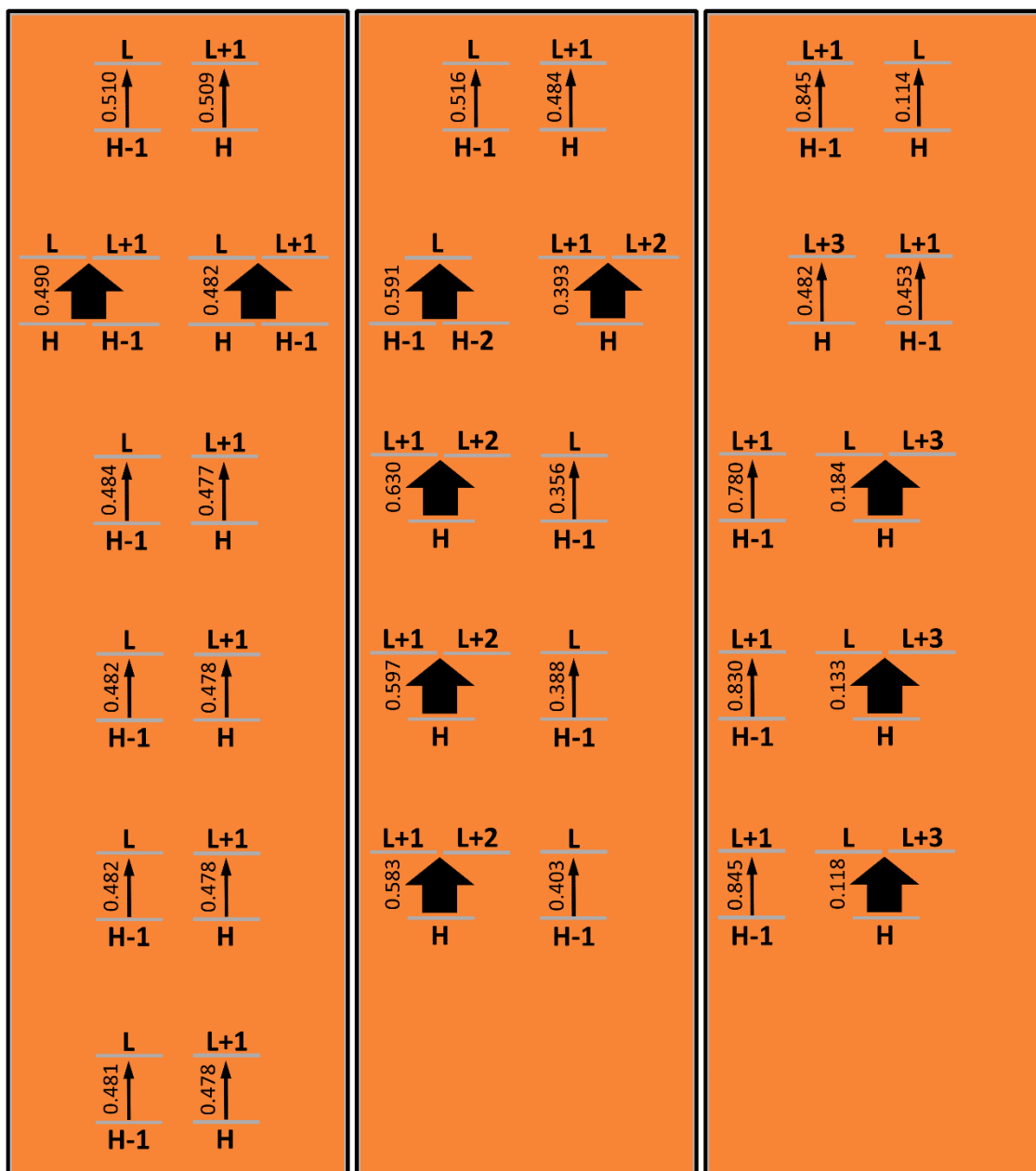
Fig 6. Occupied to virtual MO electron promotion representing the excitation modes in h-BNCs with a central benzene (left plot) or pyrene (central plot for *y*-polarized mode and right plot for *z*-polarized mode). MO schemes are shown, from top to bottom, following an increasing order in N_{BN} (Be-N_{BN}(0-5) and Py-N_{BN}(0-4)).

Additionally, the decomposition of the DD into EDOs allows interpreting electronic transitions in terms of electron transfer channels induced by the electromagnetic perturbation and formed by combination of specific occupied and virtual orbitals (see the Supplementary Information). This is particularly useful for the study of charge transfer

transitions,[46,47] herein, we are going to use this methodology to compare the electron transfer channels along the series Be-N_{BN} and Py-N_{BN}.

The information about the electron transfer channels is summarized in Fig 6. The figure shows the occupied and virtual orbitals involved in the main channels as well as the number of electrons transferred from the ground to the excited state by each channel for the excitation modes of Be-N_{BN} and Py-N_{BN} series.

In all cases, the electronic transition is composed of two channels. In Be-N_{BN}, the MOs involved in the transition are the pair of degenerated H-1 and H and the pair of degenerated L and L+1. Obviously, these are the same MOs involved in the second degenerated mode. All the nanodisks and the benzene molecule display the same MO configuration for the two channels but Be-1. This configuration corresponds to the mixing of H-1 and L in one channel and H and L+1 in the other. In Be-1, both channels are formed by the joint mixing of these four MOs, differences between them lie in the relative weight of each MO in the mixing. On the other hand, differences in the magnitude of the electron transfer in each channel are negligible for nanodisks with $N_{BN} \geq 2$, which is the result of the response confinement discussed above.

In pyrene molecule, the *y*-polarized excitation occurs by the mixing of H-1 and L in one channel and H and L+1 in the other. The *z*-polarized excitation involves the same orbitals but with different mixing, one channel is formed by H-1 and L+1 and the other channel by H and L. Once again, the introduction of the first BN string in Py-1 provokes noticeable differences with respect to the isolated hydrocarbon structure. Thus, the MO configurations of the channels change, increasing the MOs involved, namely, L+2 and L+3 in the *y*-polarized and *z*-polarized modes, respectively. For $N_{BN} \geq 2$, the MO configurations of the two excitation modes do not change among the different nanodisks but differences in the electron transfer are noticed. Thus, whereas in the Be-N_{BN} series

the electron transfer of the main channels was practically the same for nanodisks with $N_{BN} \geq 2$, in Py-N_{BN} the changes may be considered negligible only between the largest nanodisks, Py-3 and Py-4.

Surface Raman Enhancement

The electromagnetic "hot" spots located at the carbon nanoislands and their near surroundings could be exploited for electronic, magnetic or optical applications, depending upon the electronic configuration of the carbon nanoisland. In this subsection, we explore its application to the enhancement of the Raman activity of molecules adsorbed on the h-BNC surface. To this aim, we have chosen the Py-N_{BN} surface model and placed a water molecule above the center of the pyrene unit (see Fig 7). The perpendicular conformation of the symmetry axis of the water molecule with respect to the h-BNC plane is not the most stable conformation, which corresponds to a parallel disposition of the water and h-BNC planes. However, it is the most interesting one for the SERS analysis performed here since, in the perpendicular disposition, we can distinguish between perpendicular and parallel orientations of the bending vibrational mode (the most enhanced mode) with respect to the transition dipole moments associated to the *y* and *z*-polarized electronic excitations. The water-surface distance has been fixed for all the Py-N_{BN} nanodisks to that obtained in the geometry optimization of the pyrene-water complex. The surface geometries have been also fixed, allowing to reduce the changes observed in the Raman spectra to those arising from the different number of BN strings. Since the analysis has been focused on the Raman signals corresponding to the water vibrational modes, the water geometry has been fully relaxed in all cases.
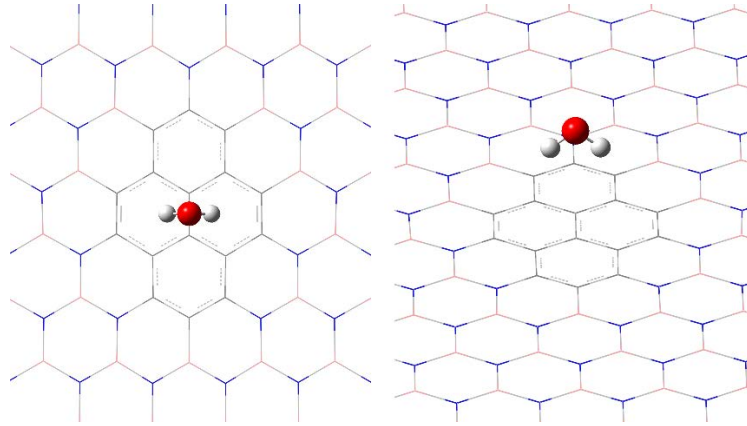
Fig 7. Representation of the Py-N$_{BN}$-water complexes from two different views.

The three Raman signals corresponding to the water molecule placed above the Py-N$_{BN}$ nanodisks ($0 \leq N_{BN} \leq 4$) are shown in Fig 8. They have been obtained using off-resonance and near-resonance conditions. For simulating near-resonance conditions, an electromagnetic perturbation of wavelength near the resonance wavelength of the *y*-polarized or the *z*-polarized excitation mode has been introduced in the calculation of the Raman activity. As mentioned in the previous section, the contributions of water and surface atoms to the Raman activity have been calculated and the former has been employed to represent hypothetical spectra where the effect of molecule-surface vibrational coupling is hidden. These hypothetical spectra have been superimposed to the full spectra in Fig 8 and will be denoted as mol-spectrum.

The bending mode is centred at 1662 cm^{-1} in the Py-0-water complex. It is slightly blue-shifted to 1665 cm^{-1} in Py-1-water but it is progressively red-shifted again when increasing the number of BN strings up to reach 1664 cm^{-1} in Py-4-water. On the contrary, the displacement of the symmetric and antisymmetric stretching mode frequencies with the number of BN strings is negligible, being centred at 3849 and 3952 cm^{-1}, respectively. The off-resonance spectra are represented on the left side of Fig 8. As it can be observed, the intensity of the bending mode increases as the nanodisk size increases, being its value

in Py-4-water three times that of Py-0-water. This increase is induced by the vibrational coupling with the surface, as reflected by the mol-spectrum, in which the bending mode tends to decrease slightly with the nanodisk size. On the contrary, the intensity of the stretching modes does not change significantly along the series and even decreases slightly from Py-0-water to Py-4-water. This is because no molecule-surface vibrational coupling is found for these modes (see the corresponding mol-spectra). These findings are in agreement with a general observation in SERS, namely, the bending modes are frequently the most enhanced by the surface. Water adsorbed on metal substrates is a well-known example of this.[42]

Upon near-resonance conditions with the y-polarized mode of the Py-N_{BN} substrate, an enhancement factor around 10^5 is observed for the bending mode signal (see the spectra in the middle column of Fig 8). This enhancement, although showing the same order of magnitude, decreases from Py-1 to Py-2 but afterwards it keeps almost constant for Py-2, Py-3 and Py-4, with a slight increase linked to the augmentation of the molecule-surface vibrational coupling already observed in the off-resonance spectra.

When the electromagnetic perturbation is close to resonance with the z-polarized mode, the effect is quite similar to the y-polarized mode discussed above, however, two details are remarkable. First, the bending signal intensities in the mol-spectra are slightly larger than those obtained for the y-polarized mode but, in the full spectra, they are noticeably smaller. The former could be explained by the larger oscillator strengths of the z-polarized mode, which is also reflected on larger LTDMs in the pyrene unit, however, the latter has no simple explanation. The intensities in the full spectra depend strongly on the molecule-surface vibrational coupling as it is manifested in Fig 8. The distribution of the excitation modes (the TDs) around the surface atoms more involved in the coupling is then crucial to understand the different enhancements observed. It is certainly not the aim of this work

to perform such a thorough analysis. The most important result extracted from this part of the study is the large Raman enhancement factors obtained for the water vibrational modes due to the proximity to the electromagnetic "hot" spots located at the pyrene nanoislands. This finding certainly points out the h-BNC hybrid 2D materials are possible candidates for SERS applications.
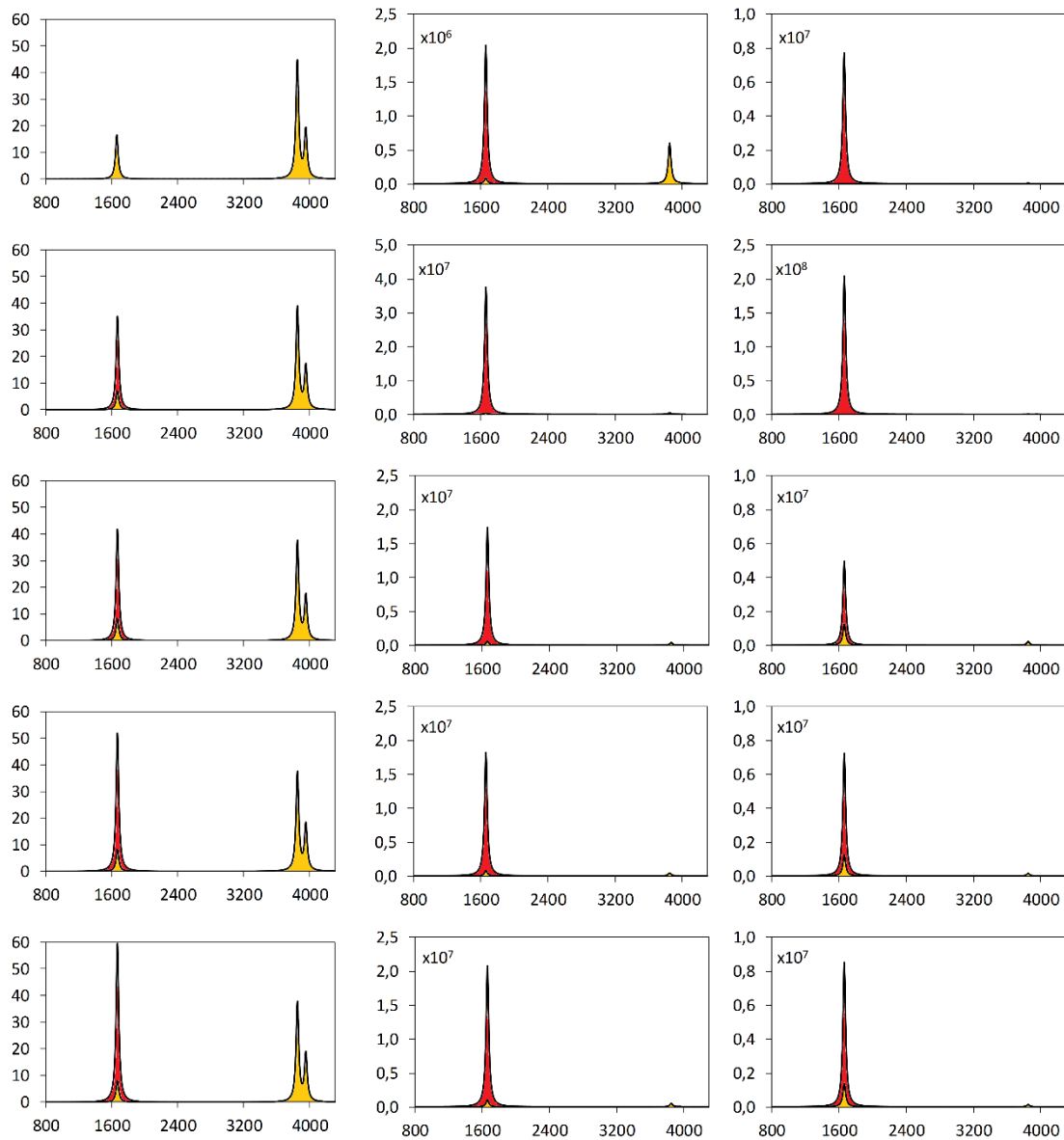
Fig 8. Simulated Raman spectra for a water molecule adsorbed on h-BNCs with central pyrene. Off-resonance spectra (left) and near-resonance spectra (central for *y*-polarized mode and right for *z*-polarized mode) are shown in the figure. Spectra are shown from top to bottom following an increasing order in N_{BN}. The full signal is shown in red whereas the contribution to the signal due to the water molecule is shown in light orange.

CONCLUSIONS

In this work, the optical confinement exerted by boron-nitride strings on carbon nanoislands within BN monolayers has been investigated using quantum chemical methods. It has been found that the "isolation" of the optical modes of the carbon nanoisland is reached after two BN strings. This result has been obtained using two different nanoisland models: benzene and pyrene. Thus, excitation wavelengths, transition electron densities, ground to excited state electron density differences and their associated electron deformation orbitals have been shown to be independent on the number of BN strings when this number is larger than two.

Under near-resonance conditions with the active optical modes of the nanoisland, Raman enhancement factors around 10^6 have been obtained for the vibrational modes of a water molecule placed over the pyrene nanoisland. This result points out the electromagnetic "hot spots" created by the BN strings could be exploited in SERS applications or related spectroscopic techniques. Moreover, the strong confinement and tunability of the optical response in h-BNCs through changes in the size and shape of the embedded carbon nanoislands makes these 2D materials more versatile than those based on charge transfer mechanisms, such as graphene or graphene oxide. This is because the charge transfer excitations are strongly dependent on the relative positions of surface and molecule energy levels, which change for different molecules.

REFERENCES

[1]   Bao, Q.; Loh, K. P. Graphene Photonics, Plasmonics, and Broadband Optoelectronic Devices. *ACS Nano* **2012**, *6*, 3677–3694.

[2]   J. C. Dong, J. C.; Li, H. Monoatomic Layer Electronics Constructed by Graphene and Boron Nitride Nanoribbons. *J. Phys. Chem. C* **2012**, *116*, 17259–17267.

[3]   Ferrari, A. C.; Bonaccorso, F.; Fal'ko, V.; Novoselov, K. S.; Roche, S.; Bøggild, P.; Borini, S.; Koppens, F. H. L.; Palermo, V.; Pugno, N.; Garrido, J. A.; Sordan, R.; Bianco, A.; Ballerini, L.; Prato, M.; Lidorikis, E.; Kivioja, J.; Marinelli, C.; Ryhänen, T.; Morpurgo, J.; Coleman, N.; Nicolosi, V.; Colombo, L.; Fert, A.; Garcia-Hernandez, M.; Bachtold, A.; Schneider, G. F.; Guinea, F.; Dekker, C.; Barbone, M.; Sun, Z.; Galiotis, C.; Grigorenko, A. N.; Konstantatos, G.; Kis, A.; Katsnelson, M.; Vandersypen, L.:; Loiseau, A.; Morandi, V.; Neumaier, D.; Treossi, E.; Pellegrini, V.; Polini, M.; Tredicucci, A.; Williams, G. M.; Hong, B. H.; Ahn, J.-H.; Kim, J. M.; Zirath, H.; van Wees, B. J.; van der Zant, H.; Occhipinti, L.; Matteo, A. D.; Kinloch, I. A.; Seyller, T.; Quesnel, E.; Feng, X.; Teo, K.; Rupesinghe, N.; Hakonen, P.; Neil, S. R. T.; Tannock, Q.; Löfwander, T.; Kinaret, J. Science and Technology Roadmap for Graphene, Related Two-Dimensional Crystals, and Hybrid Systems. *Nanoscale* **2015**, *7*, 4598–4810.

[4]   Rana, F. Graphene Terahertz Plasmon Oscillators. *IEEE Trans. Nanotech. 2008*, *7*, 91–99.

[5]   Thongrattanasiri, S.; Manjavacas, A.; García de Abajo, F.J. Quantum finite-size effects in graphene plasmons. *ACS Nano* **2012**, *6*, 1766–1775.

[6]   Manjavacas, A.; Marchesin, F.; Thongrattanasiri, S.; Koval, P.; Nordlander, P.; Sánchez-Portal, D.; García de Abajo, F.J. Tunable molecular plasmons in polycyclic aromatic hydrocarbons. *ACS Nano* **2013**, *7*, 3635–3643.

[7]   Wang, J.; Ma, F.; Sun, M. Graphene, hexagonal boron nitride, and their heterostructures: properties and applications. *RSC Adv*. **2017**, *7*, 16801-16822.

[8]   Chen, M.; Liu, D.; Du, X.; Lo, K.-H.; Wang, S.; Zhou, B.; Pan, H. 2D materials: Excellent substrates for surface-enhanced Raman scattering (SERS) in chemical sensing and biosensing. *Trends Anal. Chem.* **2020**, *130*, 115983.

[9]   Ci, L.; Song, L.; Jin, C.; Jariwala, D.; Wu, D.; Li, Y.; Srivastava, A.; Wang, Z.F.; Storr, K.; Balicas, L.; Liu, F.; Ajayan, P. M. Atomic layers of hybridized boron nitride and graphene domains. *Nat. Mater.* **2010**, *10*, 430–435.

[10] Gong, Y.; Shi, G.; Zhang, Z.; Zhou, W.; Jung, J.; Gao, W.; Ma, L.; Yang, Y.; Yang, S.; You, G.; Vajtai, R.; Xu, Q.; MacDonald, A. H.; Yakobson, B. I.; Lou, J.; Liu, Z.; Ajayan, P. M. Direct chemical conversion of graphene to boron- and nitrogen- and carbon-containing atomic layers. *Nat. Commun.* **2014**, *5*, 3193.

[11] Lorenzo-García, M.M.; Bonifazi, D. Renaissance of an Old Topic: From Borazines to BN-doped Nanographenes. *Chimia* **2017**, *71*, 550–557.

[12] Herrera-Reinoza, N.; dos Santos, A. C.; de Lima, L. H.; Landers, R.; de Siervo, A. Atomically Precise Bottom-Up Synthesis of h-BNC: Graphene Doped with h-BN Nanoclusters *Chem. Mat.* **2021**, *33*, 2871-2882.

[13] Karamanis, P.; Otero, N.; Pouchan, C. Unleashing the quadratic nonlinear optical responses of graphene by confining white-graphene (h-BN) sections in its framework. *J. Am. Chem. Soc.* **2014**, *113*, 7464–7473.

[14] Karamanis, P.; Otero, N.; Pouchan, C. Electric property variations in nanosized hexagonal boron nitride/graphene hybrids. *J. Phys. Chem. C* **2015**, *119*, 11872–11885.

[15] Otero, N.; El-Kelany, K.E.; Pouchan, C.; Rérat, M.; Karamanis, P. Establishing the pivotal role of local aromaticity in the electronic properties of boron-nitride graphene lateral hybrids. *Phys. Chem. Chem. Phys.* **2016**, *18*, 25315–25328.

[16] Bevilacqua, A. C.; Köhler, M. H.; Azevedo, S.; Baierle, R. J. Stability, and optical and electronic properties of ultrathin h-BNC. *Phys. Chem. Chem. Phys.* **2017**, *19*, 5629-5636.

[17] Gil-Guerrero, S.; Otero, N.; Queizán, M.; Mandado, M. Potential Application of h-BNC Structures in SERS and SEHRS Spectroscopies: A Theoretical Perspective. *Sensors* **2019**, *19*, 1896/1-14.

[18] L. Jensen, L.; C. M. Aikern, C.M.; G. C. Schatz, G. C. Electronic structure methods for studying surface-enhanced Raman scattering *Chem. Soc. Rev.* **2008**, *37*, 1061-1073.

[19] Chulhai, D. V.; Hu, Z.; Moore, J. E.; Chen, X.; Jensen, L. Theory of Linear and Nonlinear Surface-Enhanced Vibrational Spectroscopies *Annu. Rev. Phys. Chem.* 2016, **67**, 541-564.

[20] Ramos-Berdullas, N.; López-Carballeira, D.; Pérez-Juste, I.; Mandado, M. On the mechanism responsible of Raman enhancement on carbon allotropes surfaces: The role of molecule-surface vibrational coupling in SERS. *J. Raman. Spectrosc.* **2015**, *46*, 1205–1214

[21] Ramos-Berdullas, N.; López-Carballeira, D.; Mandado, M.; Pérez-Juste, I. Revisiting the mechanism and the influence of the excitation wavelength on the surface-enhanced Raman scattering of the pyridine–Ag20 system. *Theor. Chem. Acc.* **2015**, *134*, 60/1-13

[22] López-Carballeira, D.; Ramos-Berdullas, N.; Pérez-Juste, I.; Mandado, M. Can single graphene nanodisks be used as Raman enhancement platforms? *RSC Adv.* **2016**, *6*, 71397–71403.

[23] Nie, S. M.; Emory, S. R. Probing Single Molecules and Single Nanoparticles by Surface-Enhanced Raman Scattering. *Science* **1997**, *275*, 1102–1106.

[24] Ling, X.; Xie, L.; Fang, Y.; Xu, H.; Zhang, H.; Kong, J.; Dresselhaus, M.S.; Zhang, J.; Liu, Z. Can Graphene be used as a Substrate for Raman Enhancement? *Nano Lett.* **2010**, *10*, 553–561.

[25] Xu, W.; Mao, N.; Zhang, J. Graphene: A Platform for Surface-Enhanced Raman Spectroscopy. *Small* **2013**, *9*, 1206–1224.

[26] Ling, X.; Huang, S.; Deng, S.; Mao, N.; Kong, J.; Dresselhaus, M.S.; Zhang, J. Lighting Up the Raman Signal of Molecules in the Vicinity of Graphene Related Materials. *Acc. Chem. Res.* **2015**, *48*, 1862–1870.

[27]   Ramos-Berdullas, N.; Pérez-Juste, I.; Van Alsenoy C.; Mandado, M. Theoretical study of the adsorption of aromatic units on carbon allotropes including explicit (empirical) DFT dispersion corrections and implicitly dispersion-corrected functionals: the pyridine case. *Phys. Chem. Chem. Phys.* **2015**, *17*, 575-587.

[28]   López-Carballeira, D.; Ramos-Berdullas, N.; Pérez-Juste, I.; Cagide-Fajín, J. L.; Cordeiro, M. N. D. S.; Mandado, M. A computational study of the interaction of graphene structures with biomolecular units. *Phys. Chem. Chem. Phys.* **2016**, *18*, 15312-15321.

[29]   Xie, L.; Ling, X.; Fang, Y.; Zhang, J.; Liu, Z. Graphene as a substrate to suppress fluorescence in Resonance Raman Spectroscopy. *J. Am. Chem. Soc.* **2009**, *131*, 9890–9891.

[30]   Huang, S.; Ling, X.; Liang, L.; Song, Y.; Fang, W.; Zhang, J.; Kong, J.; Meunier, V.; Dresselhaus, M.S. Molecular Selectivity of Graphene-Enhanced Raman Scattering. *Nano Lett.* **2015**, *15*, 2892–2901.

[31]   Feng, S.; dos Santos, M. C.; Carvalho, B. R.; Lv, R.; Li, Q.; Fujisawa, K.; Elías, A. L.; Lei, Y.; Perea-López, N.; Endo, M.; Pan, M.; Pimenta, M. A.; Terrones, M. Ultrasensitive molecular sensor using N-doped graphene through enhanced Raman scattering. *Sci. Adv.* **2016**, *2*, e1600322.

[32]   Yoon, J.-C.; Thiyagarajan, P.; Ahna, H.-J.; Jang, J.-H. A case study: effect of defects in CVD-grown graphene on graphene enhanced Raman spectroscopy. *RSC Adv.* **2015**, *5*, 62772-62777.

[33]   Yang, H.; Hu, H.; Ni, Z.; Poh, C.-K.; Cong, C.; Lin, J.; Yu, T. Comparison of surface-enhanced Raman scattering on graphene oxide, reduced graphene oxide and graphene surfaces. *Carbon*. **2013**, *62*, 422-429.

[34]   Xu, W.; Ling, X.; Xiao, J.; Dresselhaus, M. S.; Kong, J.; Xu, H.; Liu, Z.; Zhang, J. Surface enhanced Raman spectroscopy on a flat graphene surface. *PNAS* **2021**, *109*, 9281-9286.

[35]   Lauchner, A.; Schlather, A. E.; Manjavacas, A.; Cui, Y.; McClain, M. J.; Stec, G. J.; García de Abajo, F. J.; Nordlander, P.; Halas, N. J. Molecular Plasmonics. *Nano Lett.* **2015**, *15*, 6208–6214.

[36]   Casademont-Reig, I.; Woller, T.; Contreras-García, J.; Alonso, M.; Torrent-Sucarrat, M.; Matito, E. New electron delocalization tools to describe the aromaticity in porphyrinoids. *Phys. Chem. Chem. Phys.* 2**018**, *20*, 2787-2796.

[37]   Limacher, P. A.; Mikkelsen, K. V.; Lüthi, H. P. On the accurate calculation of polarizabilities and second hyperpolarizabilities of polyacetylene oligomer chains using the CAM-B3LYP density functional. *J. Chem. Phys.* **2009**, *130*, 194114.

[38]   Peach, M. J. G; Tellgren, E. I.; Sałek, P.; Helgaker, T.; Tozer, D. J. Structural and Electronic Properties of Polyacetylene and Polyyne from Hybrid and Coulomb-Attenuated Density Functionals. *J. Phys. Chem. A* **2007**, *111*, 46, 11930–11935.

[39]   Gaussian 09, Revision E.01, Frisch, M. J.; Trucks, G. W.; Schlegel, H. B.; Scuseria, G. E.; Robb, M. A.; Cheeseman, J. R.; Scalmani, G.; Barone, V.; Mennucci, B.; Petersson, G. A.; Nakatsuji, H.; Caricato, M.; Li, X.; Hratchian, H.

P.; Izmaylov, A. F.; Bloino, J.; Zheng, G.; Sonnenberg, J. L.; Hada, M.; Ehara, M.; Toyota, K.; Fukuda, R.; Hasegawa, J.; Ishida, M.; Nakajima, T.; Honda, Y.; Kitao, O.; Nakai, H.; Vreven, T.; Montgomery, J. A., Jr.; Peralta, J. E.; Ogliaro, F.; Bearpark, M.; Heyd, J. J.; Brothers, E.; Kudin, K. N.; Staroverov, V. N.; Kobayashi, R.; Normand, J.; Raghavachari, K.; Rendell, A.; Burant, J. C.; Iyengar, S. S.; Tomasi, J.; Cossi, M.; Rega, N.; Millam, J. M.; Klene, M.; Knox, J. E.; Cross, J. B.; Bakken, V.; Adamo, C.; Jaramillo, J.; Gomperts, R.; Stratmann, R. E.; Yazyev, O.; Austin, A. J.; Cammi, R.; Pomelli, C.; Ochterski, J. W.; Martin, R. L.; Morokuma, K.; Zakrzewski, V. G.; Voth, G. A.; Salvador, P.; Dannenberg, J. J.; Dapprich, S.; Daniels, A. D.; Farkas, Ö.; Foresman, J. B.; Ortiz, J. V.; Cioslowski, J.; Fox, D. J. Gaussian, Inc., Wallingford CT, 2009.

[40] GaussView, Version 6, Dennington, R. D.; Keith, T. A.; Millam, J. M. Semichem Inc., Shawnee Mission, KS, 2016.

[41] Norman, P.; Bishop, D. M.; Jensen, H. J. A.; Oddershede, J. Near-resonant absorption in the time-dependent self-consistent field and multiconfigurational self-consistent field approximations. *J. Chem. Phys.* **2001**, *115*, 10323-10334.

[42] Sanchez-Lozano, M.; Mandado, M.; Pérez-Juste, I.; Hermida Ramón, J. M. Theoretical Vibrational Raman and SERS Spectra of Water interacting with Silver clusters. *ChemPhysChem* **2014**, *15*, 4067-4076.

[43] Allouche, A. R. Gabedit - A graphical user interface for computational chemistry softwares, *J. Comput. Chem.* **2011**, *32*, 174-182.

[44] Zdetsis, A. D. 4 n + 2 = 6 n? A Geometrical Approach to Aromaticity?, *J. Phys. Chem. A* **2021**, *125*, 6064-6074.

[45] Ullrich, C. A. Time-Dependent Density-Functional Theory: Concepts and Applications. Oxford University Press, New York, US, 2012.

[46] Head-Gordon, M.; Graña, A. M.; Maurice, D.; White, C. A. Analysis of electronic transitions as the difference of electron attachment and detachment densities. *J. Phys. Chem.* **1995**, *99*, 14261-14270.

[47] Dreuw, A.; Head-Gordon, M. Single-Reference ab Initio Methods for the Calculation of Excited States of Large Molecules. *Chem. Rev.* **2005**, *105*, 4009-4037.